Applied Catalysis B: Environmental 330 (2023) 122656

Contents lists available at ScienceDirect

Applied Catalysis B: Environmental

journal homepage: www.elsevier.com/locate/apcatb

Mn-Co dual sites relay activation of peroxymonosulfate for accelerated decontamination

Yiyuan Yao [1], Chaohai Wang [1], Yingpeng Yang, Shuai Zhang, Xin Yan, Chengming Xiao, Yujun Zhou, Zhigao Zhu, Junwen Qi, Xiuyun Sun, Jiansheng Li *

Jiangsu Key Laboratory of Chemical Pollution Control and Resources Reuse, School of Environmental and Biological Engineering, Nanjing University of Science and Technology, Nanjing 210094, People's Republic of China

ARTICLE INFO

Keywords:
Relay activation
Peroxymonosulfate
Dual atom catalysts
Bifunction
Enhanced degradation

ABSTRACT

Dual atomic catalysts are specially designed for relay activation of peroxymonosulfate (PMS). Here, a programmable metal-triazolate framework is utilized as a precursor to introduce the bimetallic sites (containing Mn and Co) for the synthesis of contiguous Mn−N and Co−N sites anchored on nitrogen-doped porous carbon polyhedral (MCNC). Excellent decontamination performance with TOF/PMS = 46.3 $L^2\ min^{-1}\ g^{-2}$ is observed on the MCNC, which is 1.6 and 1.5 times of single Mn and single Co catalysts. Singlet oxygen quantifying, ^{18}O isotope labeling, and theoretical simulations jointly unravel that MCNC activates PMS through a unique "relay" mode, where one site interacts with the O atom in PMS, and the other expedites producing $^1O_2$ via PMS* activation. This work advances the origin activation of PMS and enhances the removal for the refractory pollutants by rational regulation of dual site synergistic catalyst, which deepens the on-demand design of Fenton-like reaction.

1. Introduction

Peroxymonosulfate-based advanced oxidation processes (PMS-AOPs), effective approaches to generate both highly-oxidative radicals and highly-selective non-radicals, have aroused significant research interest in the areas of ever-growing environmental pollution [1,2]. Generally, the pivotal process of the PMS activation always contains two inalienable steps: (i) adsorption of PMS on catalysts; and following by (ii) the breakage of the O−O bond for generating reactive oxygen species (ROS) [3]. Currently, single-atom catalysts (SACs), realizing the leading atom-utilization efficiency and tunable electronic structures, have been regarded as excellent candidates to accelerate the PMS activation process [4,5]. Since Li firstly proposed the single Co atoms anchored on porous N-doped graphene for efficient PMS activation, [6] substantial efforts have been devoted to adjusting the electronic structure of catalyst by altering the metal center (Mn, Fe, Co, Ni, Cu, etc.) [7,8] or introducing heteroatomic doping (B, N, S, P, etc.) [9] to boost the second step of PMS activation [10]. Most importantly, the existing SACs with enhanced catalytic activity and maximal atomic utilization efficiency, only have a single top site, impeding the probability for multifunctional synergies in catalytic processes [11,12]. Besides, blindly increasing the amounts of SACs can only improve the performance to a certain, but greatly cause the problem of engineering difficulty. Therefore, under the demand of sustainable development, the design of SACs with double functional sites is urgently desired to synergetically promote the stepwise PMS activation process [13–15].

More recently, dual metal catalysts, boasting amphibious functions and electronic synergies between different metal centers, are demonstrated promising catalysts to boost PMS activation process [16,17]. The synergetic effect between bimetallic oxides of two different metal has been proposed. For example, $Mn_{1.8}Fe_{1.2}O_4$ nanospheres exhibited excellent performance in bisphenol A (BPA) removal compared with the mixtures of Fe_3O_4 and Mn_3O_4, where Mn and Fe served as the primary catalytic active site and the main substrate adsorption site, respectively [16]. Specifically, the interaction between the two metals could complement and reinforce each other, in detail, one for optimization of PMS adsorption and another for the supplement of more favorable active sites via proton-electron transfer between ROSs, thus endowing dual-metal catalysts with bifunctional properties [18]. Inspired by the asset of both SACs and bimetallic oxides, constructing dual atom catalysts

* Corresponding author.
E-mail address: lijsh@njust.edu.cn (J. Li).
[1] These authors equally contributed to this work.

https://doi.org/10.1016/j.apcatb.2023.122656
Received 9 November 2022; Received in revised form 14 March 2023; Accepted 16 March 2023
Available online 21 March 2023
0926-3373/© 2023 Elsevier B.V. All rights reserved.

(DACs) with bifunction should be an auspicious strategy to address the relay PMS activation, while still a challenge.

Specifically, metal-nitrogen (M-N) are recognized as the typical single atom active sites for effective activation of PMS through unsaturated coordination configuration. Metal-triazolate (MET) frameworks, a subclass of porous crystalline solids, demonstrate an attractive precursor for fabrication of atomic anchored nitrogen doped carbon via the pyrolysis [19,20]. The adjustable divalent metal nodes of MET with an extremely high N content creates infinite possibilities for preparation of DACs.

Based on this, we aim to systematically investigate the relay activation process of PMS via incorporating Mn and Co transition metals into a nitrogen-doped porous carbon polyhedral (MCNC) as the bimetallic active site. Intriguingly, in contrast to Co−N-doped porous carbon polyhedral (CNC) and Mn−N-doped porous carbon polyhedral (MNC), MCNC was approved to be the most catalytically reactive to initiate PMS activation, which ultimately evolved ROS. Both experimental results and theoretical simulations unravel that MCNC activate PMS through a unique "relay" mode, where one site interacts with the O atom in PMS for secondary attack, and the other Co−N expedites producing $^1O_2$ via PMS* activation. This work is expected to hoist the Fenton-like reaction by finely advancing the synergistic interaction towards dual metal centers and guiding the origin activation process of oxidants.

2. Experimental methods

2.1. Reagents

All reagents were used without purification, the detailed information was provided in Text S1 of the Supporting Information.

2.2. Synthesis of the MCNC catalysts

For the first step, the $Zn(C_2N_3H_2)_2$ (MET-6) nanoparticles were obtained by mixing solution A and B with stirring for 24 h at room temperature. The solution A comprised $ZnCl_2$ (1.0 g), ethanol (10 mL), water (15 mL), ammonium hydroxide (5 mL) and N, N-dimethylformamide (DMF, 10 mL). Solution B (1 H-1,2,3-triazole, 1.25 mL) was then added dropwise to A. After centrifuged and washed by ethanol for three times, the white precipitate was obtained following by drying at 80 °C in a vacuum oven. Secondly, $Mn(NO_3)_2$ 4 H_2O (0.72 g) and Co $(NO_3)_2$ 6 H_2O (0.63 g) were employed as the metal sources dissolving in 200 mL methanol. Then MET-6 (2.0 g) was immersed into that for continuously stirring 24 h. The obtained sample was centrifuged at 8000 rpm for 3 min and washed with methanol three times. Finally, the MCNC was prepared by pyrolysis with programmed temperature of 1 °C min^{-1} towards 1000 °C and kept for 2 h under a flowing nitrogen atmosphere. Similarly, the NC, CNC, and MNC, which were derived from carbonization of MET-6, Co@MET-6, Mn@MET-6, were synthesized according to the same procedures.

2.3. Characterization

The detailed characterization methods were described in Text S2.

2.4. Catalytic experiment and analyses

To evaluate the removal performance, a batch experiment was performed in a 100 mL mixed solution of BPA (20 mg L^{-1}), PMS (0.1 g L^{-1}) and catalyst (0.03 g L^{-1}) in a constant temperature water bath at 30 °C with 500 rpm. As the reaction proceeded, 0.75 mL aliquots of reaction solution were withdrawn by eppendoff for high-performance liquid chromatograph (HPLC) (Waters, e2695) analyzing, as described in Text S3. Also the radical quenching experiments and the quantitative analysis of chemical PMSO and the oxidative product $PMSO_2$ were conducted by the similar methods, that were listed in Text S3, 4.

3. Results and discussion

3.1. Characterization

The Mn−Co bimetal nitrogen-doped porous carbon polyhedral (MCNC) with atomic dispersion was prepared via pyrolysis, whose precursor was replaced by Mn^{2+} and Co^{2+} in situ in the metal-triazolate frameworks (MET-6) (Fig. 1a). By controlling the metal ions, the metal free NC and single-metal doped NC based on Co (CNC) or Mn (MNC) atoms were prepared. As expected, the scanning electron microscopy (SEM) and powder X-ray diffraction (PXRD) patterns synchronously confirmed that the morphology and crystal structure of MET-6 maintained unaffected by the introduction of Co and Mn (Figs. S1-S2). The sharp declines of weight loss at ≈ 400 ℃ with a sudden intense heat release indicated the decomposition of the triazole ligands, which reflected on the thermogravimetric (TG) curve (Fig. S3). The weight loss continues to decline to 1000 ℃ that selecting for further calcination in N_2. As depicted in Fig. S4 and S5, the octahedral configuration of MCNC successfully sustained after pyrolysis in 1000 ℃ under the N_2, generating sufficient hierarchical pores due to the instantaneously massive release of gas and heat [19,20]. The N_2 adsorption-desorption isotherms further confirm the presence of the rich micropores and mesopores of the MCNC, with high specific surface area of 968.6 m^2 g^{-1} and large pore volume of 1.31 cm^3 g^{-1} (Fig. S6a, Table S1). The similar pore size distributions of the NC, CNC, and MNC are also observed in Fig. S6b. which probably generating during the evaporation of Zn and the formation of N_2. The hierarchical pore structure is beneficial to mass transfer and electron transport [21]. The detailed evidence of Mn and Co atomically distribution was further uncovered by the aberration-corrected high-angle annular dark-filed scanning TEM (HAADF-STEM). The atomically dispersed bimetal on the porous carbon was elucidated by the appearance of the coupled bright spots (typically circled by boxes), attributed by the heavier atomic masses of Mn and Co than C and N (Fig. 1b). In addition, the distances of coupled spots in the randomly selected regions (red boxes of Fig. 1b) were identified by the intensity profiles (Fig. 1c), with the results of all close to 0.23 ± 0.02 nm, verifying the formation of dual atom pairs in MCNC (Fig. S7). The electron energy loss spectrum (EELS) also provided strong evidence of the neighbored Mn and Co, by verifying the Mn and Co signals on the adjacent sides (Fig. 1d). Integrated with the above analysis, such collective HAADF-STEM, energy dispersive X-ray spectroscopy (EDS) mapping, and XRD results (Fig. 1e, Fig. S8, Table S2), infer that the co-existence of Mn and Co as Mn/Co neighbors, in a form of coordinating with conjoint N, other than large particles. Additionally, the Mn and Co contents of MCNC was determined by the inductively coupled plasma atomic emission spectrometry.

(ICP-OES), turning out that the weight percentage of Mn and Co anchored on the N-doped carbon is 0.62 wt% and 0.85 wt%, respectively, while Co of CNC is 2.72 wt% and Mn of MNC is 2.22 wt% (Table S3).

X-ray photoelectron spectroscopy (XPS) was performed to investigate the chemical composition of the MCNC catalyst. As depicted in Fig. S9, after introducing of Mn/Co, the content of pyridinic N (398.4 eV) decreases compared with the NC, while a new N species appears at 399.0 eV, associated with the metal-N bond. The transformation of N species indicates that abundant atomically dispersed metal-nitrogen formed and related to the pyridinic N. The corresponding high-resolution XPS spectra for Co 2p and Mn 2p are also provided, as well as the element contents are provided in Table S2. The Co 2p spectrums of the CNC and MCNC show that only Co^{2+} (782.0 eV) and Co^{3+} (780.2 eV) exist, without Co^0. Notably, a higher oxidation state of Co is found in MCNC (Fig. S10), which indicates higher relevance toward $^1O_2$ [22]. In the Mn 2p spectrums (Fig. S11), the Mn^{2+} with 640.9 eV dominates, which increases the reduction capacity [23]. The charge density reveals electron transfer between Mn and Co center of MCNC compared with CNC and MNC, where the Co, Mn dual sites

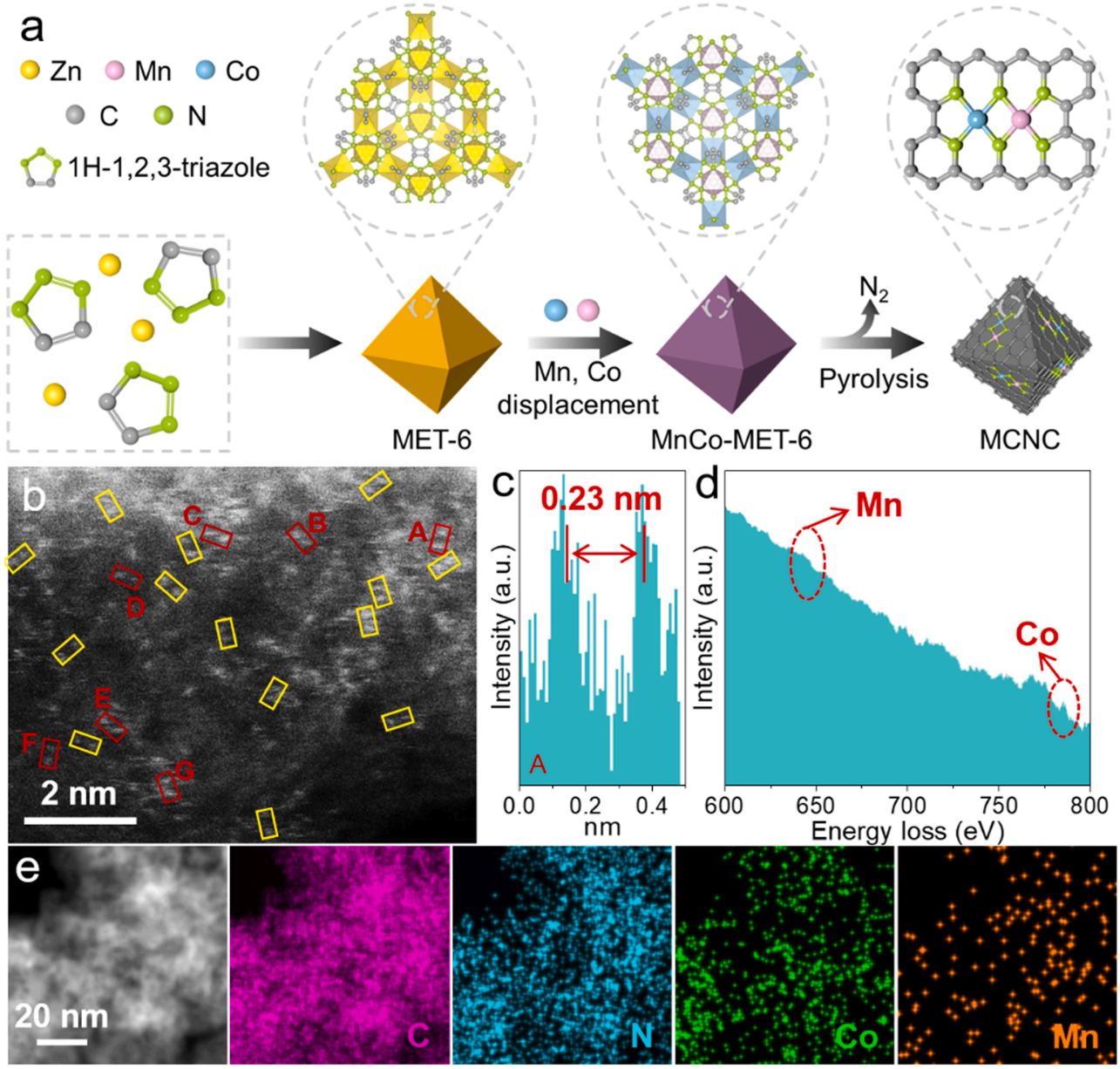

Fig. 1. (a) Schematic illustration of synthesis procedure for MCNC catalysts; (b) Aberration-corrected HAADF-STEM image and some of bimetallic Co/Mn sites are highlighted by red blocks; (c) The MCNC structure analyzed by EELS; (d) The intensity profiles obtained on two bimetallic Mn−Co sites; (e) Elements mappings of MCNC (C, N, Co, and Mn).

exhibit a slight poor electronic center in the MCNC could be observed (Fig. S12), indicating the stable anchoring of Mn and Co in the N-doped carbon [24]. The charge density is consistent with the XPS results, which preliminarily indicates the bifunction in the Fenton-like process.

To further validate the inference of the local structure and coordination environment for Mn and Co, the synchrotron-radiation-based X-ray adsorption fine structure (XAFS) analysis, including X-ray adsorption near-edge spectroscopy (XANES) and K-edge extended X-ray adsorption fine structure (EXAFS) analyses were performed. Co K-edge XANES in Fig. 2a shows that the threshold value (E_0) of the MCNC is between CoO and Co_3O_4, but closer to that of Co_3O_4, indicating that the valance of Co in the MCNC is situated below + 3.0 V. The formation of Co−N coordination in the MCNC is confirmed by the apparent peak at 1.4 Å in the Fourier transform (FT) k^3-weighted EXAFS spectra of Co K-edge (Fig. 2b), while neglectable peak corresponding to metal−metal was observed in the MCNC. As shown in Fig. 2c, the Wavelet Transform (WT) contour plots of MCNC shows only one intensity maximum at about 4.0 $Å^{-1}$ which is associated with the Co−N bond. Similarly, the Mn K-edge XANES spectra for the MCNC is located between MnO and Mn_2O_3, demonstrating a between + 2 and + 3 valence state of Mn (Fig. 2d). The EXAFS outcome (Fig. 2e) and the only intensity maximum observed at around 4 $Å^{-1}$ indexing the Mn−N coordination, further proving the uniform dispersion of single-atom Mn (Fig. 2 f). According to the least-squares EXAFS fitting results, the Co and Mn atoms in the MCNC are respectively coordinated to four N atoms ($Co-N_4$ and $Mn-N_4$) with each bond length being ~1.97 Å, whereas the rest are inferred as coordinated by O when exposed to air. Furthermore, the fitting k space curve is calculated in Fig. S13a, b, and the detailed parameter is listed in Table S4. Based on the aforementioned fitting results, the most possible Mn, $Co-N_6$ structure is illustrated in Fig. 2 g, h (inset), in accordance with the XPS conclusions (Fig. 2i). The corresponding theoretical calculation of the distance between Mn and Co of the Mn, $Co-N_6$ model is 2.3 Å, which is approximately in accord with the measured space. The proved dual atomic structure is very promising

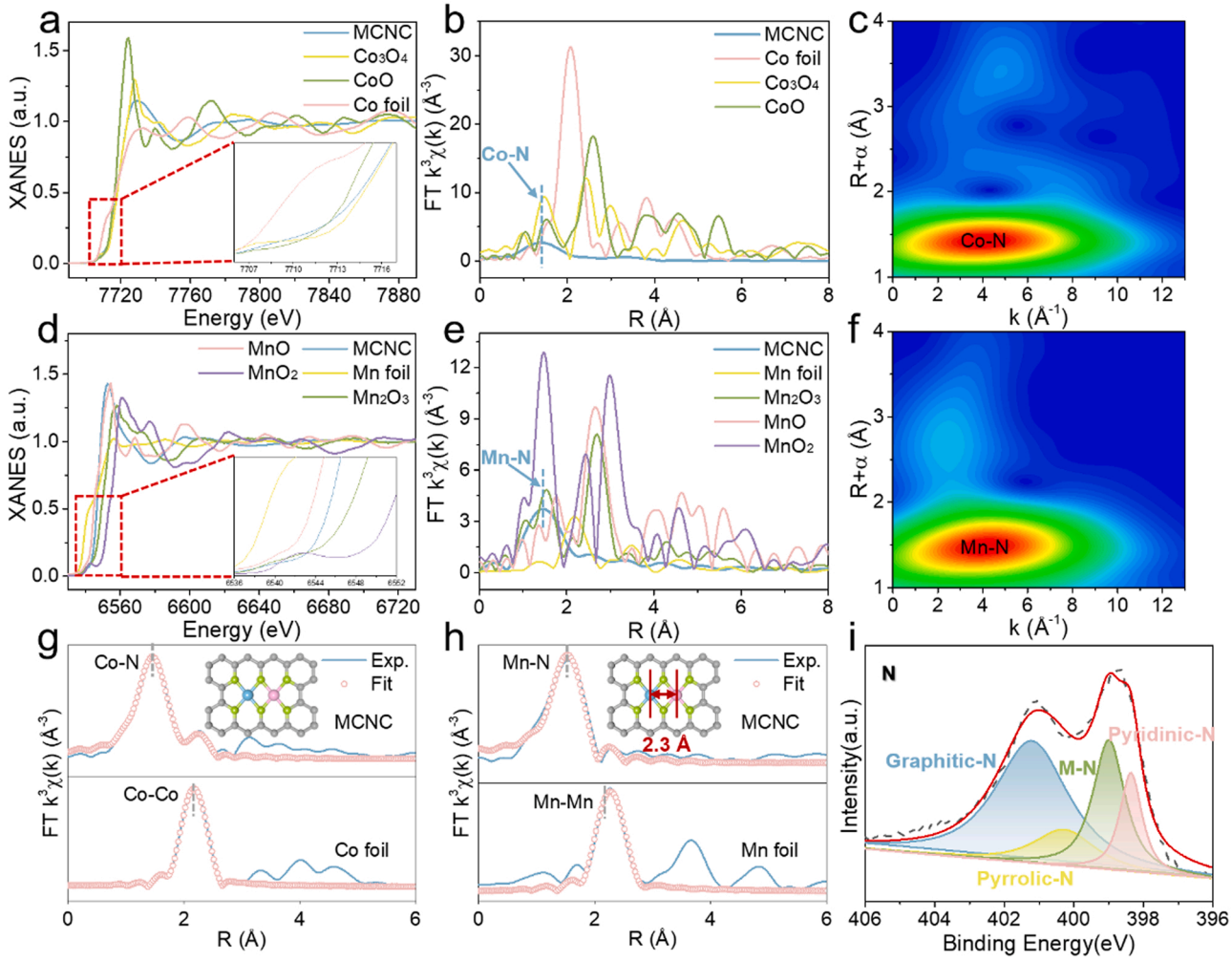

Fig. 2. (a, d) Co and Mn K-edge XANES, (b, e) Fourier-transform EXAFS spectra, and (c, f) Wavelet transform of the k^3-weighted EXAFS data of MCNC and reference samples; (g, h) Co and Mn K-edge EXAFS fitting curves; (i) High-resolution N 1 s XPS spectra of MCNC.

to stimulate PMS with the collaborating adsorption via a relay mode.

3.2. PMS activating capacity

The catalytic performance of the NC, CNC, MCNC, and MNC were intriguing to investigate in the PMS solution for BPA degradation. The control experiments show that all the samples exhibit rapid adsorptive removal on BPA of less than 20% (Fig. S14). The similar adsorption capacity can be attributable to the comparable carbon network with hierarchical pores, which provide sufficient space for pollutants and effective supports for active sites. Meanwhile, the BPA removal rate ranges from 92.5% to 99.0% with various NC catalysts under the same conditions (Fig. S15). Nevertheless, as presented in Fig. 3a, an appreciable degradation rate constant (k) of BPA is achieved in the MCNC/PMS system, which is significantly higher than the other systems. Noticeably, the physical mixture of CNC and MNC (noted as M+C) fails to improve the k value. The only distinction among the catalysts is metal, which determines the electron structure and dominates the reaction process. For ascertaining the contribution of k value to a single metal, the contribution factor A_M (M = metal) is defined in Supporting Information (Text S6). Combined the ICP results with BPA reaction dynamics, the A_{Co} and A_{Mn} is estimated to be 300 and 349 L min^{-1} g^{-1}, respectively. Based on this, the theoretical k of M+C comes out to be 0.24 min^{-1}, which is in agreement with the experimental. When the same computing methods are applied to MCNC, the calculated dynamics (k_{MnCo} = 0.14 min^{-1}) is much lower than the actual (k_{MCNC} = 0.31 min^{-1}), indicating the existence of the synergistic effect between the adjacent Mn and Co of MCNC towards PMS activation. In the comparison with previous studies, the obtained MCNC presents an outstanding reaction rate, which is normalized into per catalyst and oxidation dosage (Fig. 3b, Table S5). The effective process intensification is also applicable to PDS activation, which possesses similar O−O bonds, endowing the dual sites catalysts psionics in catalysis (Fig. S16). Compared with the NC, CNC, and MNC, MCNC performs omnipotence capacity in the initial PMS adsorption, the generation of ROS, the degradation of BPA and ultimate TOC removal (Fig. S16–18). The single site like Co−N or Mn−N is frequently solitary, resulting in an inferior performance (Fig. 3c). The kinetic enhancement in the oxidation process of MCNC indicates the critical role of the neighboring Mn and Co for catalytic PMS activation. In this regard, we further envisage that the significant interaction between Mn, Co−N_6 active sites and PMS. Thereby, in situ Raman spectroscopy and open circuit measurements were recorded to probe the initial steps of PMS activation. As.

shown in Fig. 3d, e, three typical peaks were observed at around 882, 980, and 1060 cm^{-1}, of which the middle represents SO_4^{2-}, rests are HSO_5^- of PMS. After the addition of PMS, NC/PMS system showed a weaken peak intensity without any shift, while the peak located at 882 cm^{-1} disappeared and the I_{1060}/I_{980} ratio decreased from 1.02 to 0.97 in the CNC/PMS system, to some extent, implying a faster PMS consumption. Surprisingly, a new peak emerged in the MNC/PMS system at around 836 cm^{-1}, which could be assigned to Mn−PMS* (an adsorbed state of PMS) due to the predominant role of Mn−N active sites

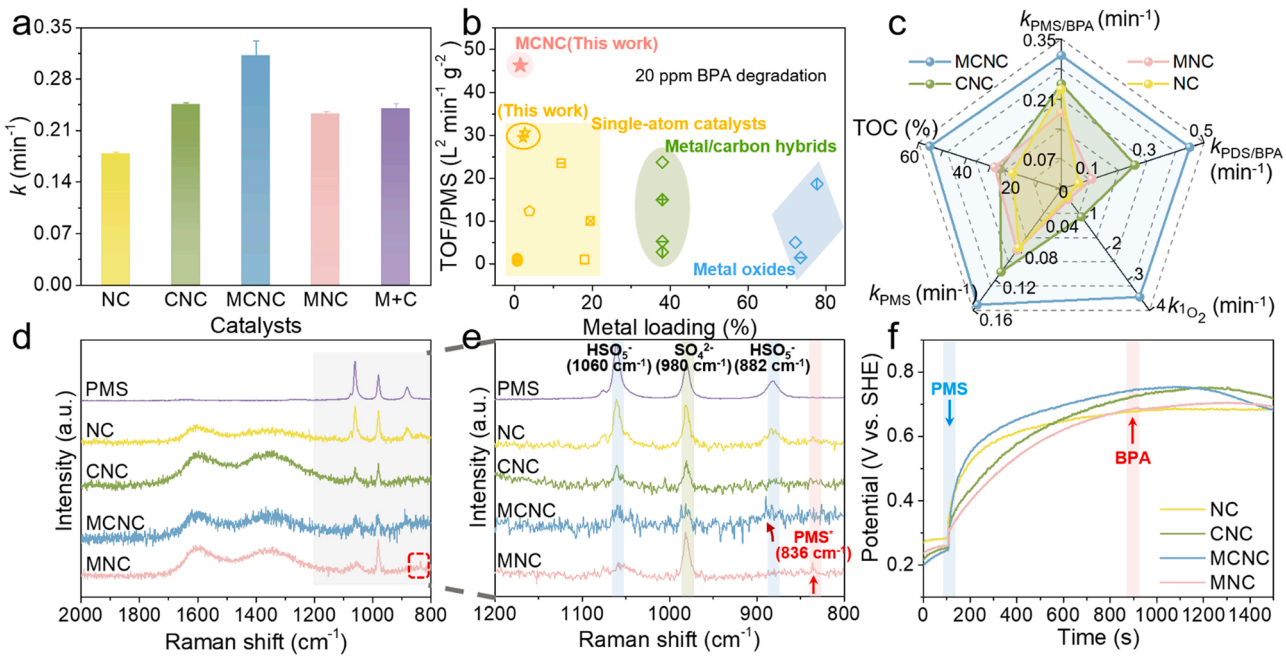

Fig. 3. (a) *k* of BPA degradation; (b) BPA decomposition by other catalysts/PMS systems; (c) Radar graph of the performance of the catalysts; (d, e) In situ Raman spectra of MCNC; (f) Open-circuit potential curves with the addition of PMS and BPA.

[8]. The metastable and highly reactive Mn−PMS* intermediate was mainly originate from the prolonged peroxo O−O bond [25]. In addition, there's no signal of Mn−PMS* could be found, but an obvious redshift of the characteristic peak of HSO_5^- was noticed (from 882 to 889 cm^{-1}), which were ascribed to the strong affinity towards the O−O bond between PMS and MCNC [26]. Moreover, the open circuit potential was performed to monitor charge migration reaction system (Fig. 3 f). The injection of PMS caused a distinct raise of the open circuit potential, following gradually balanced [25]. It was worth noting that the maximum change within the same time occurred on the MCNC competition with the others, demonstrating easier electron transfer between MCNC and PMS. When the subsequent BPA was added into the electrode solution, only little decline on the potential without a sharpen saltation, which verified the little contribution of electron transfer towards BPA degradation (Fig. S19). These results imply that the excellent performance of MCNC in the PMS/BPA system is most probably a consequence of the synergistic effect between Mn and Co active sites, where the previous adsorption of the precursor of ROS governs the intrinsic activity, followed by an enhanced removal capacity towards prompt activation of the unstable PMS*. The further relay activation process controlled by the synergistic Mn, Co dual sites could be explained by the mechanism analysis.

3.3. Determination of reactive oxygen species

The MCNC displayed the outstanding BPA degradation performance via a relay PMS activation process. However, the synergistic catalytic mechanism remained unsure. The involvement of ROSs in the MCNC/PMS/BPA system are identified as radicals or $^1O_2$, which has been widely corroborated by previous reports related by single atom Co−N active sites [22]. Therefore, a series of scavenging experiments have been conducted to verify which ROS dominates in the MCNC/PMS/BPA system. As depicted in Fig. S20a, if MeOH, TBA, or phenol was added into the reaction system, the BPA removal was negligibly influenced, which convincingly eliminated the participation of $SO_4^{\bullet-}$ and $^{\bullet}OH$, including surface-bound $SO_4^{\bullet-}$ and $^{\bullet}OH$. In addition, *L*-his was required to selectively screen $^1O_2$, in which an obvious inhibition effect towards BPA degradation was observable (Fig. S21a). Considering that the quench agent of $^1O_2$ might have effluence towards the PMS activation, the results were uncertain to judge the contribution of $^1O_2$ in the system. Therefore, the PMS consumption in the system before and after the addition of quench agent was compared. As despited in Fig. S21b, over the MCNC/PMS system, the residual PMS was slightly reduced after adding an equal molar concentration of *L*-his, with the consumption rate of PMS increasing from 0.15 min^{-1} to 0.20 min^{-1}. The only *L*-his would also decompose about 14% PMS without the presence of MCNC. For further confirming the role of $^1O_2$, D_2O was employed to replace deionized water for extending the lifetime of $^1O_2$. The accelerated removal rate of BPA in D_2O compared with the initial, proposing $^1O_2$ the primary reactive species in the system (Fig. S21c, d). It is noted that more than 92% of $^1O_2$ was detected in the MCNC/PMS system, along with the drastic top $^1O_2$ yielding rate (3.55 min^{-1}) compared with CNC (0.92 min^{-1}) and MNC (0.34 min^{-1}) (Fig. 4b). Typically, the intrinsic acceleration may be ascribed to the brisk and efficient production of $^1O_2$, following rapid decomposition to the targeted pollutant. The origin and the possible directions of $^1O_2$ have also been verified by EPR, quenching, and probe methods. The N_2 atmosphere slightly decrease the degradation rate of BPA, suggesting that the dissolved oxygen may also contribute to $^1O_2$, but not the leading ROS (Fig. S22a). Besides, the addition of *p*-BQ and the further utilization of nitro blue tetrazolium chloride monohydrate (NBT) excluded the contribution of $O_2^{\bullet-}$ (Fig. S20b) [27,28]. By using DMPO for trapping oxidizing species, no signals were observed, representing the negligible roles of radicals ($SO_4^{\bullet-}$ and $^{\bullet}OH$) or high valent metal-oxo species (Fig. S24) [29]. The results were also consistent with the in situ Raman, where witnessed the surface interaction are only PMS*, not high valent metal-oxo [30]. Another evidence provided by the distinctive three-line pattern originating from the EPR signals of TEMP-$^1O_2$ also indicates that the contribution of $^1O_2$ has vital influence to do with the degradation of BPA [31]. Interestingly, the signal intensity of TEMPO-e^- diminished considerably after adding MCNC, indicating the strong interaction between PMS and the active sites (Fig. 4c) [32]. The strong interaction between PMS and active sites mainly infers to the appetency with the O from PMS, which is comparable to the O_2 adsorption, as performed by the temperature programmed desorption of O_2 (O_2-TPD) [33]. The obvious O_2 desorption peaks with the temperature of maximum adsorption were expressed in

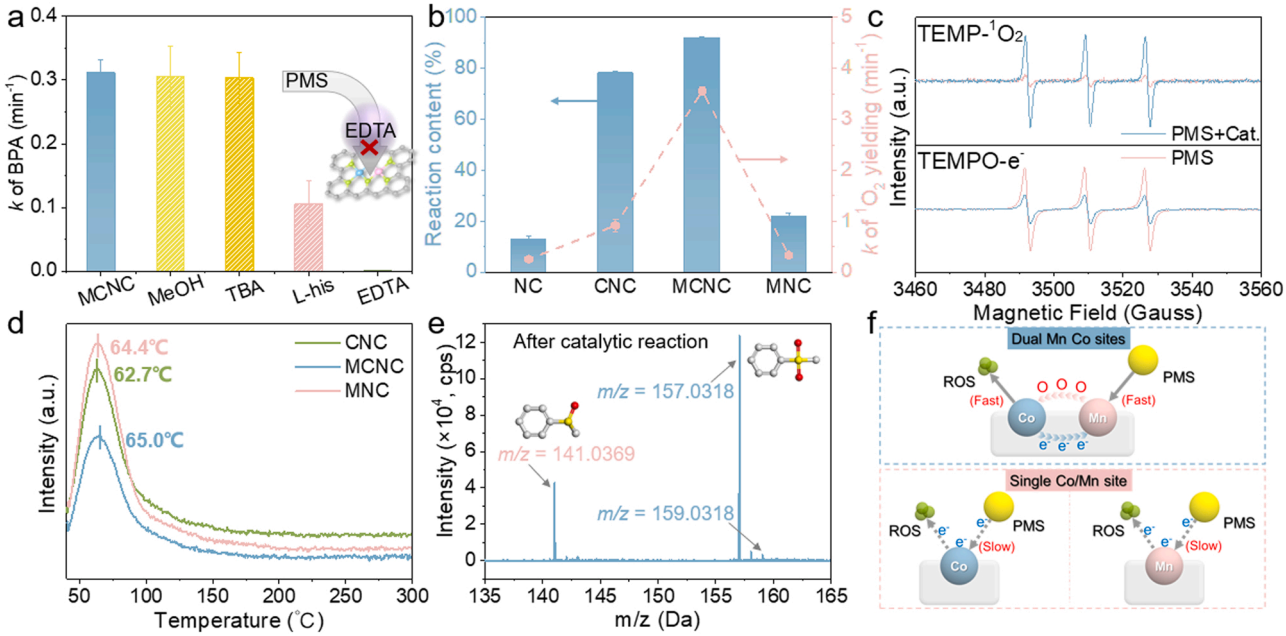

Fig. 4. (a) Quenching tests on BPA degradation by MCNC-activated PMS process; (b) The content of $^1O_2$ and kinetic studies of various samples in $^1O_2$ generation; (c) EPR test; (d) O_2-TPD; (e)The molecular ion mass spectra of PMSO and $PMSO_2$ after the catalytic reaction, respectively; (f) Possible reaction process between PMS and dual Mn, Co−N_6 active sites.

the orderliness: MCNC > MNC > CNC, indicative of the order of electron affinity of oxygen. The stronger bonding between O_2 and MCNC further indicated that an anticipate adsorption of the precursor of ROS more probable to occur. For better understanding of the active sites that dominated the reaction, the poisoning experiment that using ethylenediaminetetraacetic acid (EDTA) as the complexing reagent was conducted, which further demonstrated the Mn, Co−N_6 active sites played a pivotal role in PMS activation (Fig. 4a). Furthermore, it is essential to explore the reason of the accelerated BPA degradation rate and drastic.

$^1O_2$ production. When DMSO was added in the system, more than 30% inhibition could be observed in Fig. S22b. The inhibitory effect might be caused by the hindering of surface reactions, indicating the possibility of the surface oxygen transfer process [34]. The conjecture of O transfer pathway was further identified via PMSO, whose product could be detected as $PMSO_2$ [35,36]. The results in Fig. S23 show that almost 80% of oxidized PMSO is converted to $PMSO_2$ in the MCNC system, which is far higher than the others. As reported in previous studies, [37,38] the $^1O_2$ would directly result in PMSO to $PMSO_2$, not all of it from oxygen transfer process. Thus, an intuitive process that achieved by ^{18}O labeling technique was conducted (Fig. S25). As proved, the metal−O bond could exchange the O atom during the solvent reaction [39]. Thus, the PMSO-based LC-MS method was conducted for studying the behavior of ^{18}O in the $H_2^{18}O$ matrix (Fig. 4e). Integrated with the quantitative and qualitative analysis of the products, the production of $PMS^{16}O^{18}O$ was observed in the MCNC/PMS system. The results go straight to the point that the occurrence of O transfer, with the ^{18}O embedded into $PMSO_2$. Finally, the actual contribution of ROS in MCNC/PMS/BPA system is estimated by the comprehensive assessment of k [40]. Obviously, the contributions of $^{\bullet}OH$, $SO_4^{\bullet-}$, and surface-bound radicals are 2.5%, 1.9%, and 0%, respectively (Table S6). The top contribution (66.2%) is achieved by $^1O_2$, which also laterally verified by the secondary oxygen transfer process. The contribution value of each ROS only provides a relative value, as the quenching process might be interfered each other, such as the contribution towards BPA degradation ordered by O transfer process is overestimated, whose quenching agent is affected by $^1O_2$. As demonstrated, the PMS activation on the single metal atom almost has no synergistic effect on the relay reaction, so as to only walk on one leg, which hardly to improve the performance. On the contrary, the neighbored Mn and Co active sites are anticipated to the cohesive interrelationship that accomplish the promotion of $^1O_2$ generation along with the enhanced performance [41]. The concrete detail might be presumed to an efficient O transfer process with corrosponding electron transfer, resulting a quick relay PMS activation as illustrated in Fig. 4f.

3.4. Theoretical calculations

To delve into the catalytical discrepancies and synergies of the Mn-Co catalysis activities, the overall stimulation steps from PMS to $^1O_2$ were thermodynamically analyzed by DFT. The projected density of states (DOS) is shown in Fig. 5a, where an obvious peak of MCNC is located at the Fermi level, while for CNC and MNC are close to zero, indicating a tight electronic coupling between Mn and Co in MCNC. Comparatively, the increasing D-band center of MCNC are displayed in Fig. 5b, which facilitates the electronic conductivity and offers active sites for PMS adsorption and activation. The charge density difference and corresponding adsorption energies (E_{ads}) of PMS show that the localized electrons and the delocalized charge accumulates along the metal center, implying a strong binding for PMS molecule on Mn, Co−N_6(Mn) sites (Fig. 5c). Generally, the PMS activation to ROS is a process calling for electron transfer and PMS* is usually regarded as potential determining intermediate. The adsorption energy of PMS* formation on Mn sites in MCNC (Mn, Co−N_6(Mn)) is − 2.3 eV, much lower than their adjacent Co sites (Mn, Co−N_6(Co); − 1.9 eV) as well as CoN_4 (−2.1 eV; Fig. S26). The results above unambiguously demonstrate that the oxidative performance of Co sites.

is greatly enhanced via their adjacent Mn sites. Moreover, the reaction energy changes for $^1O_2$ production, as the primary reactive species for BPA removal, are further investigated. Based on the existing mechanism and previous work, we can conclude that the $^1O_2$ generation path is inclined to react with respect to: PMS*→OH*→O*→$^1O_2$ [7]. Therefore, the Gibbs free energies of the intermediates with certained adsorption configuration for the reaction process are calculated by DFT. The crucial step for the whole process of PMS activation is PMS adsorption, causing the elongated O−O band for breaking, closely

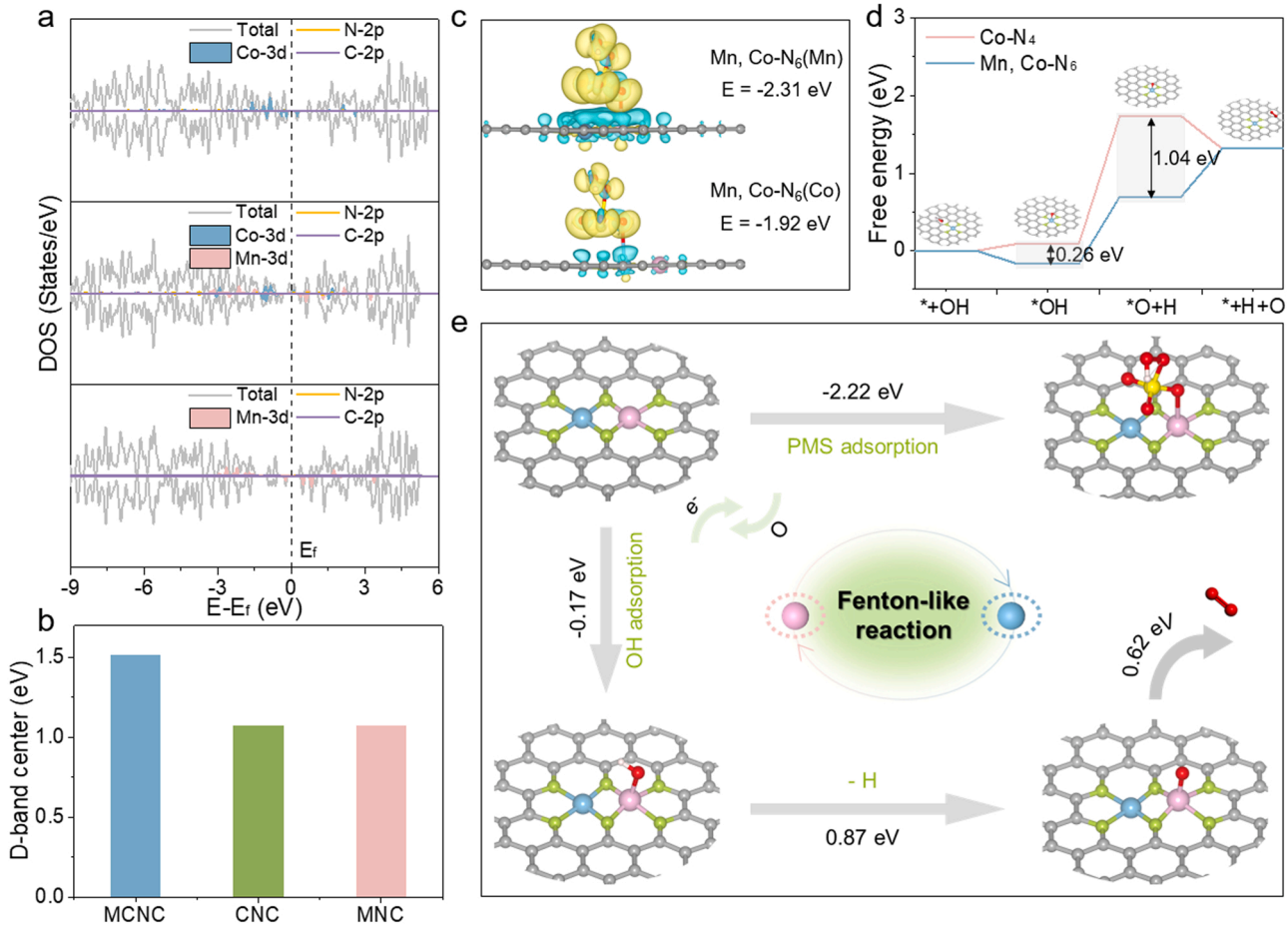

Fig. 5. DFT calculations of the PMS activity on the catalysts. (a) The DOS (the Fermi level is set to 0 in all cases), and (b) the calculated D-band of CNC, MCNC, and MNC; (c) Differential charge density of PMS adsorption model on Mn, Co−N_6(Mn) and Mn, Co−N_6(Co); The pathway and optimized atomic structures for the main process of the PMS activation on (d) CNC (Co−N_4) and (e) MCNC (Mn, Co−N_6), respectively.

accompanied by electron transportation and O transfer by the neighbored Mn−Co sites (Fig. S27). The lower free energy well confirms the point that MCNC has obvious advantages over the CNC site in terms of achieving the relay activation of PMS via the pathway of OH*→O* (Fig. 5d and Fig. S28). Significantly, the DFT results also illustrate the possibility of the formation of $^1O_2$ and the detachment of surface-adsorbed reactive species from the active sites, thus uncovering the remarkable promotion towards Fenton-like activity of the dual metal catalysts (Fig. 5e).

3.5. Demonstration of the catalytic reactor

Further investigations were conducted to illustrate the good environmental adaption of MCNC. As depicted in Fig. S29a, the general HCO_3^-, $H_2PO_4^-$, Cl^- and NO_3^- with 20 mM concentration have insubstantial impact on the performance. More importantly, MCNC achieved above 90% removal of BPA in natural (tap water and the wastewater) waters (Fig. S29b). indicating its strong anti-interference capability. As shown in Fig. S30, a significant deactivation of the MCNC on the third cyclic tests, while recovered its performance after re-pyrolysis. This is mainly due to the degradation process where by-products cover the active site and prevent further reactions,[42] verifying by the XPS results of MCNC after reaction (Fig. S31). Luckily, the active sites are re-exposed and properties are restored after pyrolysis. The leaching issue is also considered and resolved in MCNC (Table S7). Moreover, the nano-sized MCNC has been proved compelling advantage towards destroying pollutants via PMS activation due to its cooperative active sites together with feasible porous structure. However, the intrinsic powder state of engineered nanomaterials critically impedes the practical application for the difficulty in recovery. To address this issue, a MCNC loading nanofiber (MCNF) was fabricated by electrospinning to explore the applicability of MCNC. The MCNF, whose inside is consisted of energetic precursors and the outside is comprised by confined polyacrylonitrile (PAN) nanofiber, contributes to uniform porous distribution as well as accessible active sites during the pyrolysis process (Fig. S32). Besides, the macroscopically one-dimensional fiber provides a highway for electron transport and mass transfer. The advantage of the nanofiber that loaded by MCNC could be summarized in two aspects: activity and stability [43]. Utilizing the thin film state in macroscopic, the MCNF was employed into an immobilized filter.

(Fig. 6a). When the speed of the peristaltic pump was 0.1 r/min, the rhodamine B (RhB) removal achieved more than 93% even after 300 min (Fig. 6b), which demonstrated the long-term operation and easy separation recovery capacity of the catalyst.

4. Conclusion

In summary, the interaction between Mn and Co which significantly affects Fenton-like reaction reactivity, has been experimentally and theoretically demonstrated. The bimetal MCNC catalysts pronounce the relay PMS activation via the crucial PMS adsorption and subsequently ROS generation on the neighboring Mn and Co sites, emphasizing the consequence of matching the relay reaction process with the synergistic active sites in dual atom catalysts. This work unveils atomic-level insight into the collaboration of the bi-metal towards relay reaction process, which may motivate new inspiration for the on-demand design of multi-

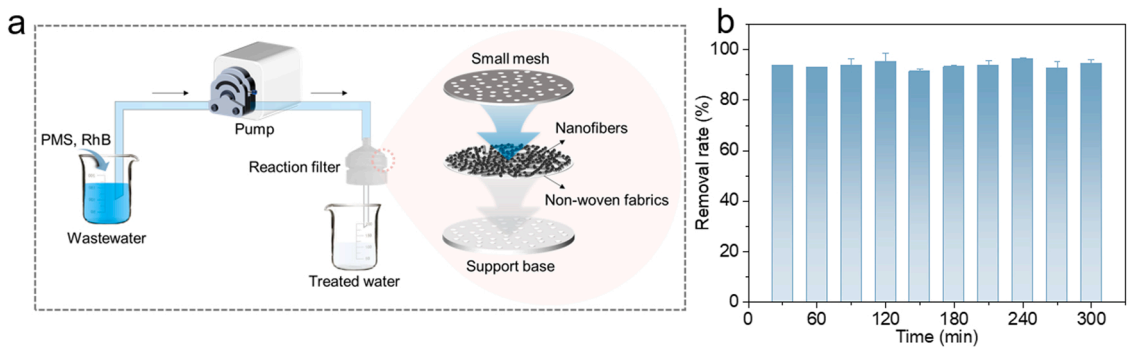

Fig. 6. (a) Schematic diagram of reaction device; (b) The RhB degradation in the MCNF/PMS system. ([RhB] = 10 ppm; [PMS] = 0.1 g L^{-1}).

metal reciprocity for efficient Fenton-like applications.

CRediT authorship contribution statement

Yiyuan Yao: Conceptualization, Methodology, Data curation, Visualization, Investigation, Writing – original draft. **Chaohai Wang**: Conceptualization, Methodology, Investigation, Validation. **Yingpeng Yang**: Methodology, Formal analysis. **Shuai Zhang**: Software, Data curation. **Xin Yan**: Software, Validation. **Chengming Xiao**: Formal analysis, Data curation. **Yujun Zhou**: Visualization, Resources. **Zhigao Zhu**: Resources. **Junwen Qi**: Investigation, Supervision. **Xiuyun Sun**: Investigation, Visualization. **Jiansheng Li**: Conceptualization, Writing – review & editing, Supervision, Project administration, Funding acquisition.

Declaration of Competing Interest

The authors declare that they have no known competing financial interests or personal relationships that could have appeared to influence the work reported in this paper.

Data availability

Data will be made available on request.

Acknowledgements

This work was finally supported by the National Natural Science Foundation of China (No. 22276096, 22206080), and the Natural Science Foundation of Jiangsu Province (BK20220969).

Appendix A. Supporting information

Supplementary data associated with this article can be found in the online version at doi:10.1016/j.apcatb.2023.122656.

References

[1] W. Ren, C. Cheng, P. Shao, X. Luo, H. Zhang, S. Wang, X. Duan, Origins of electron-transfer regime in persulfate-based nonradical oxidation processes, Environ. Sci. Technol. 56 (2022) 78–97.
[2] X. Duan, H. Sun, S. Wang, Metal-free carbocatalysis in advanced oxidation reactions, Acc. Chem. Res. 51 (2018) 678–687.
[3] X. Wu, J.-H. Kim, Outlook on single atom catalysts for persulfate-based advanced oxidation, ACS EST Eng. 2 (2022) 1776–1796.
[4] X. Mi, P. Wang, S. Xu, L. Su, H. Zhong, H. Wang, Y. Li, S. Zhan, Almost 100% peroxymonosulfate conversion to singlet oxygen on single-atom CoN_{2+2} sites, Angew. Chem. Int. Ed. 60 (2021) 4588–4593.
[5] L. Zhang, X. Jiang, Z. Zhong, L. Tian, Q. Sun, Y. Cui, X. Lu, J.P. Zou, S. Luo, Carbon nitride supported high-loading Fe single-atom catalyst for activating of peroxymonosulfate to generate $^1O_2$ with 100% selectivity, Angew. Chem. Int. Ed. 60 (2021) 21751–21755.
[6] X. Li, X. Huang, S. Xi, S. Miao, J. Ding, W. Cai, S. Liu, X. Yang, H. Yang, J. Gao, J. Wang, Y. Huang, T. Zhang, B. Liu, Single cobalt atoms anchored on porous N-doped graphene with dual reaction sites for efficient Fenton-like catalysis, J. Am. Chem. Soc. 140 (2018) 12469–12475.
[7] Y. Gao, T. Wu, C. Yang, C. Ma, Z. Zhao, Z. Wu, S. Cao, W. Geng, Y. Wang, Y. Yao, Y. Zhang, C. Cheng, Activity trends and mechanisms in peroxymonosulfate-assisted catalytic production of singlet oxygen over atomic metal-N-C catalysts, Angew. Chem. Int. Ed. 60 (2021) 22513–22521.
[8] J. Miao, Y. Zhu, J. Lang, J. Zhang, S. Cheng, B. Zhou, L. Zhang, P.J.J. Alvarez, M. Long, Spin-state-dependent peroxymonosulfate activation of single-atom M–N moieties via a radical-free pathway, ACS Catal. 11 (2021) 9569–9577.
[9] X. Zhou, M.K. Ke, G.X. Huang, C. Chen, W. Chen, K. Liang, Y. Qu, J. Yang, Y. Wang, F. Li, H.Q. Yu, Y. Wu, Identification of Fenton-like active Cu sites by heteroatom modulation of electronic density, Proc. Natl. Acad. Sci. USA 119 (2022), e2119492119.
[10] Y. Shang, X. Xu, B. Gao, S. Wang, X. Duan, Single-atom catalysis in advanced oxidation processes for environmental remediation, Chem. Soc. Rev. 50 (2021) 5281–5322.
[11] X. Liang, N. Fu, S. Yao, Z. Li, Y. Li, The progress and outlook of metal single-atom-site catalysis, J. Am. Chem. Soc. 144 (2022) 18155–18174.
[12] J. Xu, X. Zheng, Z. Feng, Z. Lu, Z. Zhang, W. Huang, Y. Li, D. Vuckovic, Y. Li, S. Dai, G. Chen, K. Wang, H. Wang, J.K. Chen, W. Mitch, Y. Cui, Organic wastewater treatment by a single-atom catalyst and electrolytically produced H_2O_2, Nat. Sustain. 4 (2021) 233–241.
[13] Z. Yang, J. Qian, C. Shan, H. Li, Y. Yin, B. Pan, Toward selective oxidation of contaminants in aqueous systems, Environ. Sci. Technol. 55 (2021) 14494–14514.
[14] Y.J. Zhang, G.X. Huang, L.R. Winter, J.J. Chen, L. Tian, S.C. Mei, Z. Zhang, F. Chen, Z.Y. Guo, R. Ji, Y.Z. You, W.W. Li, X.W. Liu, H.Q. Yu, M. Elimelech, Simultaneous nanocatalytic surface activation of pollutants and oxidants for highly efficient water decontamination, Nat. Commun. 13 (2022) 3005.
[15] Y. Wei, J. Miao, P.J.J. Alvarez, M. Long, How to accurately assess the intrinsic activity of catalysts in peroxy activation? Environ. Sci. Technol. 56 (2022) 10557–10559.
[16] G.X. Huang, C.Y. Wang, C.W. Yang, P.C. Guo, H.Q. Yu, Degradation of bisphenol A by peroxymonosulfate catalytically activated with $Mn_{1.8}Fe_{1.2}O_4$ nanospheres: synergism between Mn and Fe, Environ. Sci. Technol. 51 (2017) 12611–12618.
[17] Z. Guo, C. Li, M. Gao, X. Han, Y. Zhang, W. Zhang, W. Li, Mn−O covalency governs the intrinsic activity of Co−Mn spinel oxides for boosted peroxymonosulfate activation, Angew. Chem. Int. Ed. 60 (2021) 274–280.
[18] A. Wang, J. Ni, W. Wang, D. Liu, Q. Zhu, B. Xue, C.-C. Chang, J. Ma, Y. Zhao, MOF derived Co−Fe nitrogen doped graphite carbon@crosslinked magnetic chitosan micro−nanoreactor for environmental applications: synergy enhancement effect of adsorption−PMS activation, Appl. Catal. B Environ. 319 (2022), 121926.
[19] R. Zhao, Z. Liang, S. Gao, C. Yang, B. Zhu, J. Zhao, C. Qu, R. Zou, Q. Xu, Puffing up energetic metal-organic frameworks to large carbon networks with hierarchical porosity and atomically dispersed metal sites, Angew. Chem. Int. Ed. 58 (2019) 1975–1979.
[20] L. Hu, C. Dai, L. Chen, Y. Zhu, Y. Hao, Q. Zhang, L. Gu, X. Feng, S. Yuan, L. Wang, B. Wang, Metal-triazolate-framework-derived FeN_4-Cl_1 single-atom catalysts with hierarchical porosity for the oxygen reduction reaction, Angew. Chem. Int. Ed. 60 (2021) 27324–27329.
[21] Z. Zhao, L. Duan, Y. Zhao, L. Wang, J. Zhang, F. Bu, Z. Sun, T. Zhang, M. Liu, H. Chen, Y. Yang, K. Lan, Z. Lv, L. Zu, P. Zhang, R. Che, Y. Tang, D. Chao, W. Li, D. Zhao, Constructing unique mesoporous carbon superstructures via monomicelle interface confined assembly, J. Am. Chem. Soc. 144 (2022) 11767–11777.
[22] Y. Yao, C. Wang, X. Yan, H. Zhang, C. Xiao, J. Qi, Z. Zhu, Y. Zhou, X. Sun, X. Duan, J. Li, Rational regulation of Co–N–C coordination for high-efficiency generation of $^1O_2$ toward nearly 100% selective degradation of organic pollutants, Environ. Sci. Technol. 56 (2022) 8833–8843.
[23] X. Li, Z. Ao, J. Liu, H. Sun, A.I. Rykov, J. Wang, Topotactic transformation of metal-organic frameworks to graphene-encapsulated transition-metal nitrides as efficient Fenton-like catalysts, ACS Nano 10 (2016) 11532–11540.
[24] X. Zheng, Y. Liu, Y. Yan, X. Li, Y. Yao, Modulation effect in adjacent dual metal single atom catalysts for electrochemical nitrogen reduction reaction, Chin. Chem. Lett. 33 (2022) 1455–1458.
[25] W. Ren, L. Xiong, X. Yuan, Z. Yu, H. Zhang, X. Duan, S. Wang, Activation of peroxydisulfate on carbon nanotubes: electron-transfer mechanism, Environ. Sci. Technol. 53 (2019) 14595–14603.

[26] Y. Chen, G. Zhang, H. Liu, J. Qu, Confining free radicals in close vicinity to contaminants enables ultrafast Fenton-like processes in the interspacing of MoS_2 membranes, Angew. Chem. Int. Ed. 58 (2019) 8134–8138.
[27] C. Song, Q. Zhan, F. Liu, C. Wang, H. Li, X. Wang, X. Guo, Y. Cheng, W. Sun, L. Wang, J. Qian, B. Pan, Overturned loading of inert CeO_2 to Active Co_3O_4 for unusually improved catalytic activity in Fenton-like reactions, Angew. Chem. Int. Ed. 61 (2022), e202200406.
[28] C. Zhu, Y. Nie, S. Zhao, Z. Fan, F. Liu, A. Li, Constructing surface micro-electric fields on hollow single-atom cobalt catalyst for ultrafast and anti-interference advanced oxidation, Appl. Catal. B Environ. 305 (2022), 121057.
[29] S. Wu, W. Wu, J. Fan, L. Zhang, Y. Zhong, H. Xu, Z. Mao, Rapid activation of peroxymonosulfate with iron(III) complex for organic pollutants degradation via a non-radical pathway, Water Res. 233 (2023), 119725.
[30] C. Cheng, W. Ren, F. Miao, X. Chen, X. Chen, H. Zhang, Generation of Fe(IV)=O and its contribution to Fenton-like reactions on a single-atom iron-N-C catalyst, Angew. Chem. Int. Ed. 62 (2023), e202218510.
[31] M. Zhang, J. Ruan, L. Wang, Z. Zhao, W. Shao, J. Li, Z. Chen, C. Gu, W. Qiao, MXene-like carbon sheet/carbon nanotubes derived from metal-organic frameworks for efficient removal of tetracycline by non-radical dominated advanced oxidation processes, Sep. Purif. Technol. 300 (2022), 121851.
[32] S. Ma, D. Yang, Y. Guan, Y. Yang, Y. Zhu, Y. Zhang, J. Wu, L. Sheng, L. Liu, T. Yao, Maximally exploiting active sites on Yolk@shell nanoreactor: nearly 100% PMS activation efficiency and outstanding performance over full pH range in Fenton-like reaction, Appl. Catal. B Environ. 316 (2022), 121594.
[33] G. Yang, J. Zhu, P. Yuan, Y. Hu, G. Qu, B.A. Lu, X. Xue, H. Yin, W. Cheng, J. Cheng, W. Xu, J. Li, J. Hu, S. Mu, J.N. Zhang, Regulating Fe-spin state by atomically dispersed Mn−N in Fe−N−C catalysts with high oxygen reduction activity, Nat. Commun. 12 (2021) 1734.
[34] J. Wang, B. Li, Y. Li, X. Fan, F. Zhang, G. Zhang, W. Peng, Facile synthesis of atomic Fe-N-C materials and dual roles investigation of Fe-N_4 sites in Fenton-like reactions, Adv. Sci. 8 (2021) 2101824.
[35] H. Li, Z. Zhao, J. Qian, B. Pan, Are free radicals the primary reactive species in Co (II)-mediated activation of peroxymonosulfate? New evidence for the role of the Co (II)-peroxymonosulfate complex, Environ. Sci. Technol. 55 (2021) 6397–6406.
[36] B. Wang, C. Cheng, M. Jin, J. He, H. Zhang, W. Ren, J. Li, D. Wang, Y. Li, A site distance effect induced by reactant molecule matchup in single-atom catalysts for Fenton-like reactions, Angew. Chem. Int. Ed. 61 (2022), e202207268.
[37] J. Yao, N. Wu, X. Tang, Z. Wang, R. Qu, Z. Huo, Methyl phenyl sulfoxide (PMSO) as a quenching agent for high-valent metal-oxo species in peroxymonosulfate based processes should be reconsidered, Chem. Eng. J. Adv. 12 (2022), 100378.
[38] Z. Wan, Y. Cao, Z. Xu, X. Duan, S. Xu, D. Hou, S. Wang, D.C.W. Tsang, Revealing intrinsic relations between Cu scales and radical/nonradical oxidations to regulate nucleophilic/electrophilic catalysis, Adv. Funct. Mater. (2023) 2212227.
[39] F. Chen, L.L. Liu, J.H. Wu, X.H. Rui, J.J. Chen, Y. Yu, Single-atom iron anchored tubular g-C_3N_4 catalysts for ultrafast Fenton-like reaction: Roles of high-valency iron-oxo species and organic radicals, Adv. Mater. 34 (2022) 2202891.
[40] Y. Chen, X. Bai, Y. Ji, T. Shen, Reduced graphene oxide-supported hollow Co_3O_4@N-doped porous carbon as peroxymonosulfate activator for sulfamethoxazole degradation, Chem. Eng. J. 430 (2022), 132951.
[41] M. Yang, K. Wu, S. Sun, J. Duan, X. Liu, J. Cui, S. Liang, Y. Ren, Unprecedented relay catalysis of curved Fe_1–N_4 single-atom site for remarkably efficient $^1O_2$ generation, ACS Catal. 13 (2023) 681–691.
[42] X. Guo, H. Zhang, Y. Yao, C. Xiao, X. Yan, K. Chen, J. Qi, Y. Zhou, Z. Zhu, X. Sun, J. Li, Derivatives of two-dimensional MXene-MOFs heterostructure for boosting peroxymonosulfate activation: enhanced performance and synergistic mechanism, Appl. Catal. B Environ. 323 (2023), 122136.
[43] C. Wang, J. Kim, M. Kim, H. Lim, M. Zhang, J. You, J.-H. Yun, Y. Bando, J. Li, Y. Yamauchi, Nanoarchitectured metal-organic framework-derived hollow carbon nanofiber filters for advanced oxidation processes, J. Mater. Chem. A 7 (2019) 13743–13750.